

**Experimental charge density of LiBD<sub>4</sub> from maximum entropy method**

F. Buchter,<sup>\*</sup> Z. Lodziana, A. Remhof, Ph. Mauron, O. Friedrichs, A. Borgschulte, and A. Züttel<sup>†</sup>  
*Empa, Swiss Federal Laboratories for Materials Testing and Research, Laboratory for Hydrogen and Energy,  
 Überlandstrasse 129, CH-8600 Dübendorf, Switzerland*

Y. Filinchuk

*European Synchrotron Radiation Facility, Swiss-Norwegian Beamlines, BP 220, F-38043 Grenoble, France*

L. Palatinus

*Laboratoire de Cristallographie, Le Cubotron, Ecole Polytechnique Fédérale de Lausanne, CH-1015 Lausanne, Switzerland*

(Received 31 August 2010; published 22 February 2011)

We report on maximum entropy method study of the experimental atomic and ionic charges of LiBD<sub>4</sub> in its low-temperature orthorhombic phase. Synchrotron radiation x-ray powder diffraction data, neutron powder diffraction data, and density functional calculations were used. The atomic and ionic charges were determined for both experimental and theoretical results using the Bader analysis for atoms in molecules. The charge transfer from the Li cation to the BD<sub>4</sub> anion is 0.86(±9) e, which is in good agreement with the *ab initio* calculated value of 0.895 e. The experimental accuracy was determined considering the differences between results obtained for data collected at 10 and 90 K, different experimental setups (high-resolution diffractometer or image plate diffractometer), and different structural models used for the prior density distributions needed for accurate maximum entropy calculations (refined using only synchrotron radiation x-ray powder diffraction data or combined with neutron powder diffraction data).

DOI: [10.1103/PhysRevB.83.064107](https://doi.org/10.1103/PhysRevB.83.064107)

PACS number(s): 61.66.Fn, 61.05.fm, 61.05.cp, 71.15.Mb

**I. INTRODUCTION**

Among different techniques to store hydrogen,<sup>1–5</sup> solid-state hydrogen storage in alkali, alkaline-earth, and transition-metal tetrahydroborates  $M(\text{BH}_4)_n$  ( $M = \text{Li, Na, K, Mg, Ca, Sc, Ti, Zn, Zr, Al, etc.}; n = 1, 2, 3, 4$ ) is the focus of a lot of interest because of the high hydrogen content of these compounds.<sup>3–6</sup> Some of the most promising tetrahydroborates [Li(BH<sub>4</sub>), Ca(BH<sub>4</sub>)<sub>2</sub>, and Mg(BH<sub>4</sub>)<sub>2</sub>] exhibit high decomposition temperatures related to either thermodynamic or kinetic reasons.<sup>3–6</sup> Beside kinetics, the key issue for controlling the temperature of hydrogen release in tetrahydroborates (i.e., their stability) is to act on the strength of the B-H covalent bond. Understanding the parameters and phenomena driving the B-H bond strength allows us to control the stability of tetrahydroborates.

The role played by the anionic charge in the BH<sub>4</sub> stability has recently been pointed out by several authors.<sup>2,7–10</sup> Complementary to works directly considering the role of the anionic electronic density,<sup>9,10</sup> further support was brought by works considering either the decomposition temperature  $T_{\text{dec}}$  or formation enthalpy  $\Delta H_0$  of selected tetrahydroborates with respect to the Pauling electronegativity  $\chi$  of the constituting cations  $M$ .<sup>2,7,8</sup> An illustration of the practical ability of such a relationship to suggest the choice of cation or combination of mixed cations matching an expected  $T_{\text{dec}}$  was provided recently for the first mixed-alkali tetrahydroborates<sup>11</sup> (disregarding segregation issues and assuming an average Pauling electronegativity of the two individual cations).

The x-ray diffraction data carry the information about the electronic charge density in the observed structure factors  $F_{\text{obs}}(\mathbf{H})$  extracted from the measured reflection intensities. Therefore,  $\mathbf{H} = h\mathbf{a} + k\mathbf{b} + l\mathbf{c}$  is the lattice vector of the

reflection, where  $\mathbf{a}, \mathbf{b}$ , and  $\mathbf{c}$  are the basic vectors of the reciprocal lattice and  $h, k$ , and  $l$  are the Miller indices. In principle, the electronic charge density in the unit cell is the direct Fourier transform of an infinity of  $F_{\text{obs}}(\mathbf{H})$ . Practically, the wavelength used in the experiment limits the information available by fixing the number of measured  $F_{\text{obs}}(\mathbf{H})$ ; hence, the Fourier transform is affected by series-termination errors (e.g., unphysical local minima of the density with negative charge may occur). In addition, growing a single crystal of alkali tetrahydroborate is very difficult, and powder samples were used in the present work. Compared to single-crystal diffraction, the powder averaging of the diffraction data further reduces the information contained in it. These two limitations in the available information ( $\sin \theta / \lambda \approx 0.6 \text{ \AA}^{-1}$  and powder diffraction data) prevent a reasonable use of multipole refinement of the density distribution in the unit cell. Therefore, the maximum entropy method<sup>12–16</sup> (MEM) was used to maximize the information extracted from the intrinsically limited experimental data and to determine the corresponding electronic charge distribution in the lattice, while ensuring the positivity of the distribution. It has already been demonstrated that synchrotron radiation x-ray powder diffraction (SR-XPD) data may be used to determine electronic charge density distributions using MEM.<sup>16–20</sup> Such distributions are of high enough quality to discuss disorder, thermal displacements, and, as in the present work, integrated atomic charges.<sup>16–20</sup> As part of Bayesian statistics, the MEM makes use of prior information on the system. Prior information is provided in the present case by the electronic distribution corresponding to a refined independent-atom model (IAM) using the same experimental data.<sup>16,20,21</sup> In the MEM, the unit cell is divided into a grid of  $N_p = N_a \times N_b \times N_c$  pixels. The entropy of the

system is defined as

$$S = - \sum_{i=1}^{N_p} \rho_i \ln(\rho_i/\tau_i),$$

considering the density  $\rho_i$  of each pixel and its prior density  $\tau_i$ . The prior density  $\tau_i$  introduces the prior information that we have about the system before the MEM calculation into the entropy. The  $\rho_i$  are adjusted so that  $S$  is maximized under the constraint

$$\chi^2 = \sum_{hkl} \frac{|F_{\text{obs}}(\mathbf{H}) - F_{\text{MEM}}(\mathbf{H})|^2}{\sigma_{\text{obs}}(\mathbf{H})^2} = C,$$

where  $F_{\text{MEM}}(\mathbf{H})$  are the structure factors corresponding to the final calculated distribution  $\rho$  and  $C$  is the total number of individual reflections. Moments higher than the second moment  $\chi^2$  might be used under certain circumstances.<sup>26</sup> It is worth keeping in mind that the experimental data are introduced in the MEM via  $F_{\text{obs}}(\mathbf{H})$  and  $\sigma_{\text{obs}}(\mathbf{H})$  and also via the prior distribution  $\tau$  obtained from the refinement of an IAM model. Therefore, unless additional information is introduced in this model (e.g., considering neutron diffraction data complementary to x-ray data for the refinement of the structural model), MEM consists simply of a more subtle and complete use of the experimental diffraction data, which are, in principle, model-free if the experimental data are of sufficient quality [i.e.,  $F_{\text{obs}}(\mathbf{H})$  and  $\sigma_{\text{obs}}(\mathbf{H})$  are independent of the IAM model].

In addition to the methodological precautions required for an appropriate use of MEM<sup>16,20-27</sup> (use of prior density distribution, order and distribution of normalized residuals, and priorly derived F constraints), particularities related to the investigated system, which is composed of light atoms, and the experimental instrumental setup that was used imposed additional considerations. This is particularly important for choosing an appropriate refined IAM for the treatment of the overlapped diffraction peaks and providing the prior density distribution for the MEM calculations. The difficulty here is the slight inadequacy of the IAM for hydrogen atoms consisting of a single valence electron (no core electron) involved in a covalent bond with boron.

In the present work, we report on the experimental determination of the electronic charge density of LiBD<sub>4</sub> in its low-temperature orthorhombic phase using SR-XPD data and MEM (to date, four phases are reported<sup>28</sup> for LiBH<sub>4</sub>). Two different instrumental setups have been considered because of their specific characteristics: (1) a high-resolution powder diffractometer for reducing peak overlap and (2) an image plate area detector diffractometer for the accuracy of the measured intensities and the high signal to noise ratio. Integrated ionic charges of the Li cation and BD<sub>4</sub> anion as well as the charges of individual atoms have been determined by applying Bader analysis<sup>29</sup> to the experimental electronic charge distribution. The accuracy of the experimental charges has been evaluated by comparing integrated atomic charges obtained for the different measurement temperatures, instrumental setups, and the combination of data [used to refine the structural model providing the prior distribution and used to extract  $F_{\text{obs}}(\mathbf{H})$  from the data]. Experimental results are discussed on the same

basis and are compared to density functional theory (DFT) calculated electronic density distribution.

## II. EXPERIMENT

The powder of LiBD<sub>4</sub> (purity > 95%) was purchased from Katchem Ltd., and the samples were always handled in either in vacuum or in inert atmosphere (argon or helium). All the measurements were performed using the same sample batch, except for the neutron powder diffraction (NPD) data at 10 K, which were obtained from a previous work on LiBD<sub>4</sub>.<sup>30</sup> SR-XPD data were collected at 90 K using a MAR345 image plate detector at the Swiss-Norwegian beamlines (SNBL-BM01A) at the European Synchrotron Radiation Facility in Grenoble (France). The sample was poured into 0.7-mm-diameter glass capillaries, the wavelength was 0.711710 Å, and the temperature was controlled by an Oxford Cryostream 700+ blower (90 K was the lower accessible temperature for this setup). Data were collected at three different detector-sample distances (150, 200, and 300 mm). SR-XPD data were collected at 10 and 90 K using the high-resolution powder diffractometer of the material science (MS) beamline at the Swiss Light Source (SLS) at the Paul Scherrer Institute (PSI) in Villigen (Switzerland). The samples were poured into 1.0-mm-diameter glass capillaries, the wavelength was 0.954795 Å, and the temperature was controlled by a Janis He-flow cryostat with integrated spinner. NPD data were collected at 90 K using the high-resolution powder diffractometer for thermal neutrons (HRPT) at the Swiss Spallation Neutron Source at the PSI. The samples were poured into a double-walled vanadium cylinder with a 9-mm outer diameter, 7-mm inner diameter, and 50-mm length; the wavelength was 1.494 Å; and the temperature was controlled by means of a closed-cycle He refrigerator mounted in an evacuated aluminum vessel. The absorption correction coefficient  $\mu R = 0.225$  was determined by transmission measurements.

The structural model of the orthorhombic low-temperature phase<sup>30-34</sup> of LiBD<sub>4</sub> was refined using the program FULLPROF<sup>35</sup> (version 3.80) using either SR-XPD data or combined SR-XPD and NPD data (see details of the refinement in the supplemental material<sup>36</sup>). The phased observed structure factors  $F_{\text{obs}}(\mathbf{H})$  resulting from the refinement (with corresponding standard deviation) were corrected for anomalous dispersion<sup>17</sup> and were used for the MEM calculations. When SR-XPD data from the image plate detector are used,  $F_{\text{obs}}(\mathbf{H})$  corresponding to low scattering angles are extracted from the largest detector-sample distance data (300 mm), and  $F_{\text{obs}}(\mathbf{H})$  corresponding to intermediate and high scattering angles are extracted from the middle and shortest detector-sample distance data (200 and 150 mm), respectively. Doing so optimizes the data collection by improving the resolution of the low  $\sin\theta/\lambda$  reflections (the reflections most affected by charge distributions far from the nucleus, i.e., involved in covalent bonds) while still covering a sufficient  $\sin\theta/\lambda$  range. To reduce well-known artifacts of MEM resulting from series-termination errors,<sup>23,27</sup> the refined models were used to generate a density distribution corresponding to a procrystal,<sup>37</sup> which was used as a prior distribution for MEM calculations. The MEM calculations were performed using the software BAYMEM.<sup>38</sup> A 144 × 88 × 140 pixel grid along

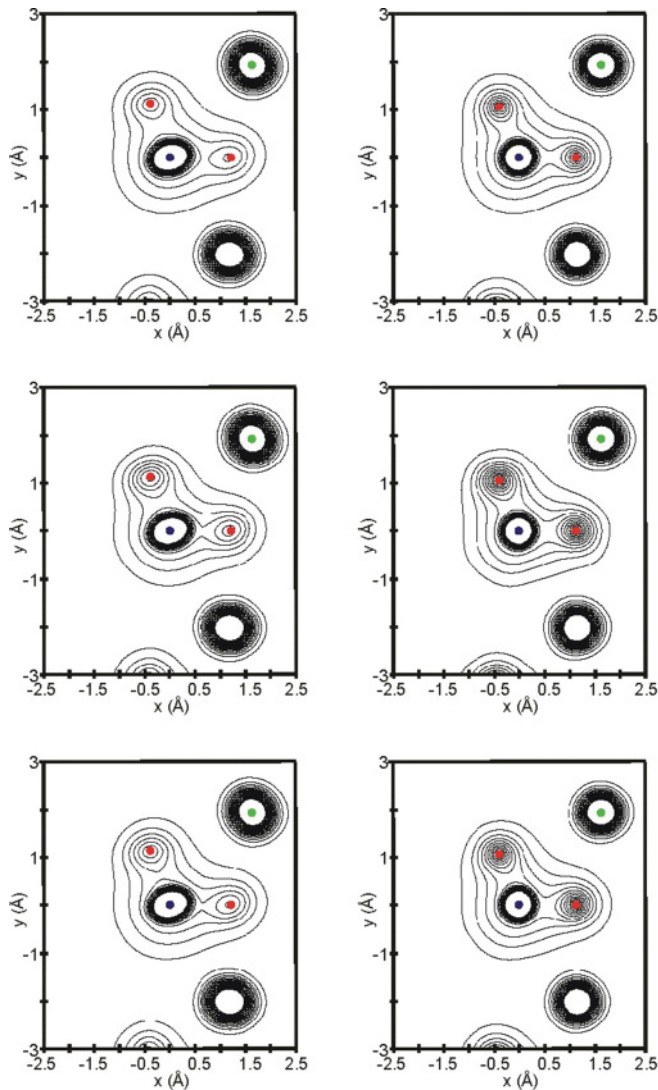


FIG. 1. (Color online) MEM density distribution for SR-XPD data at 10 K. The diffraction pattern was recorded using the high-resolution powder diffractometer of the material science (MS) beamline at the Swiss Light Source (SLS). (left)  $F_{\text{obs}}(\mathbf{H})$  from combined SR-XPD and NPD refined model. (right)  $F_{\text{obs}}(\mathbf{H})$  from SR-XPD refined model. (top) Prior density distribution, (middle) MEM density distribution with G constraint, and (bottom) MEM density distribution with G constraints. Contour intervals are  $0.2 \text{ e}/\text{\AA}^3$ ; cutoff level is  $5 \text{ e}/\text{\AA}^3$ . Plane cuts D1, D2, and B atoms; Li is green (light gray); B is blue (dark gray); D is red (medium gray).

the crystallographic axes  $a$ ,  $b$ , and  $c$  was used for MEM calculations, corresponding to  $\sim 0.05 \text{ \AA}$  of pixel resolution in each direction (i.e., the shortest interatomic distances correspond to  $\sim 25$  pixels). The resulting density distributions are presented in Figs. 1–3.

In the supplemental material<sup>36</sup> we discuss the influence of the following factors on the final MEM density distribution: (1) The intrinsic influence of the refined structural model on sharing the total intensity of a group of overlapping reflections among individual reflections, using G constraints<sup>40</sup> (i.e., with and without considering strongly overlapping reflections<sup>39</sup> as single group-structure factors  $G_{\text{obs}}(\mathbf{H})$ , called G groups). (2) The prior density distribution considering different structural

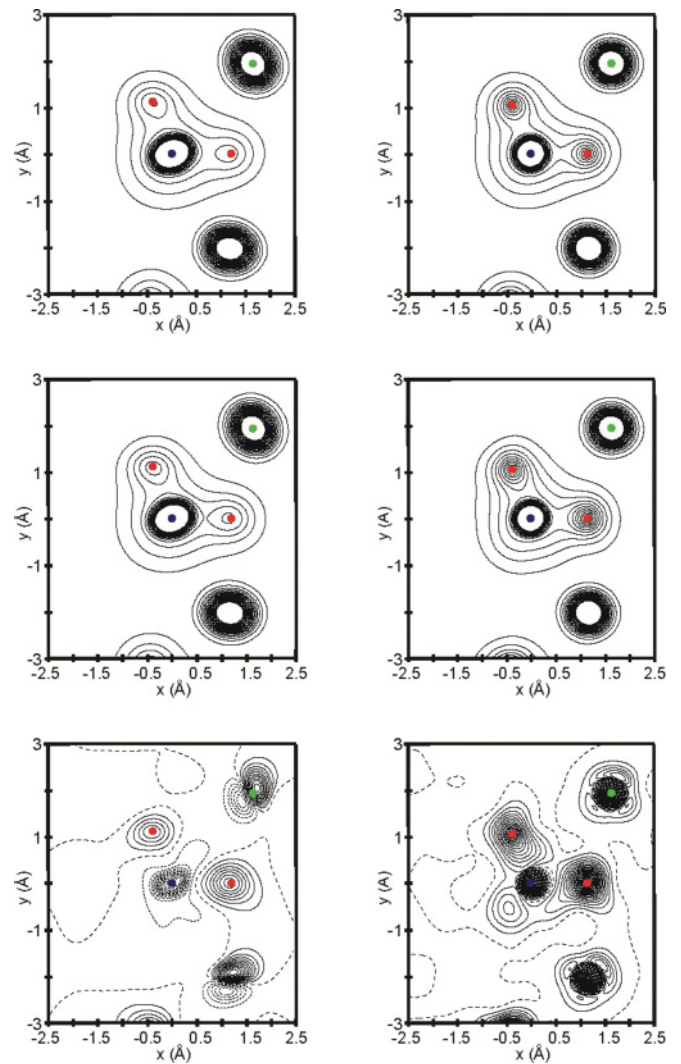


FIG. 2. (Color online) MEM density distribution for SR-XPD data at 90 K. The diffraction pattern was recorded using the high-resolution powder diffractometer of the material science (MS) beamline at the Swiss Light Source (SLS). (left)  $F_{\text{obs}}(\mathbf{H})$  from combined SR-XPD and NPD refined model. (right)  $F_{\text{obs}}(\mathbf{H})$  from SR-XPD refined model. (top) Prior density distribution, (middle) MEM density distribution with G constraint, and (bottom) difference of final minus prior. Contour intervals are  $0.2 \text{ e}/\text{\AA}^3$ ; cutoff level is  $5 \text{ e}/\text{\AA}^3$ . Contour intervals for difference plot are  $0.02 \text{ e}/\text{\AA}^3$ . Plane cuts D1, D2, and B atoms; Li is green (light gray); B is blue (dark gray); D is red (medium gray).

models for a given set of  $F_{\text{obs}}(\mathbf{H})$ . (3) The order of the statistical central moment of the normal residuals of the structure factors.<sup>26</sup> (4) The use of additional prior information from the refined structural models for higher scattering angles  $\sin \theta/\lambda \geq 0.6 \text{ \AA}^{-1}$ , via priorly derived F constraints.<sup>27</sup>

MEM distribution at 10 K (i.e., at the lowest temperature where thermal smearing of the true electronic charge is minimized) is compared to DFT-calculated electronic density distributions. Details about DFT calculation of LiBD<sub>4</sub> are extensively described elsewhere.<sup>30</sup> The DFT-calculated structures were optimized either with constrained symmetry, until the forces exerted on atoms were smaller than  $0.01 \text{ eV}/\text{\AA}$  (where the corresponding shape and volume of

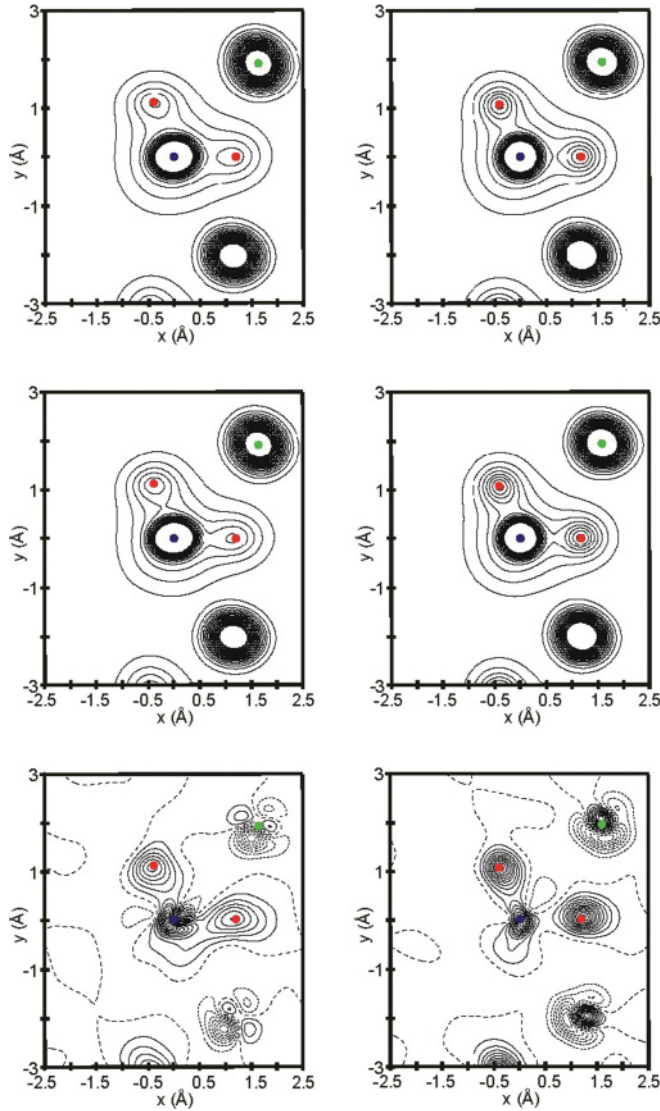


FIG. 3. (Color online) MEM density distribution for SR-XPD data at 90 K. The diffraction pattern was recorded using a MAR345 image plate detector at the Swiss-Norwegian beamline (SNBL-BM01A) at the European Synchrotron Radiation Facility. (left)  $F_{\text{obs}}(\mathbf{H})$  from combined SR-XPD and NPD refined model. (right)  $F_{\text{obs}}(\mathbf{H})$  from SR-XPD refined model. (top) Prior density distribution, (middle) MEM density distribution with G constraint, and (bottom) difference of final minus prior. Contour intervals are  $0.2 \text{ e}/\text{\AA}^3$ ; cutoff level is  $5 \text{ e}/\text{\AA}^3$ . Contour intervals for difference plot are  $0.02 \text{ e}/\text{\AA}^3$ . Plane cuts D1, D2, and B atoms; Li is green (light gray); B is blue (dark gray); D is red (medium gray).

the unit cell were relaxed and the procedure was repeated until self-consistency was achieved), or with the unit cell size and nucleus kept fixed at the experimental values of the refined structural model.

Atomic charges were subsequently determined by applying the Bader analysis for atoms in molecules to the MEM and DFT distribution,<sup>29</sup> using the program EDMA<sup>38</sup> (see Tables I–III). Atomic basins in the MEM or DFT distributions are determined by this method, considering a division of the distribution into subsystems separated by zero-density flux surfaces. Critical points<sup>29</sup> of the density distribution (i.e., points

where the density gradient vanishes) corresponding to the local maxima of the density are attributed to the basin in which they are found and are linked to the closest atom of the structural model lying in this basin. Finally, the integrated charge within a basin is fully attributed to the corresponding atom.

### III. RESULTS AND DISCUSSION

In the first part of this section, technical aspects of the MEM calculations of the electronic density distribution of light complex hydrides are discussed. In the second part, the electronic density distribution and integrated atomic and ionic charges of  $\text{LiBD}_4$  are discussed.

#### A. MEM calculations

The main factor influencing the final MEM distributions is the choice of an appropriate structural model to generate the prior distribution used in the MEM calculations (see Figs. 1–3 and Table I). To some extent, this reflects the degree of inaccuracy in the data (see supplemental material<sup>36</sup>).

In order to understand the major differences between the prior density distributions resulting from structural refinements using SR-XPD data or combined SR-XPD and NPD data, one has to consider the covalent bond involving the light atoms B and D in the  $\text{BD}_4$  tetrahedra. In the B-D covalent bond, part of the electronic charge of the B and D atoms is shared. This implies a difference between the center of mass of the atomic nucleus (CMN), which is close to the real atomic center of mass, and the center of mass of the atomic electronic distributions (CMED). In the present case, refining the  $\text{LiBD}_4$  structural model using SR-XPD data results in atomic positions close to the CMED. For the heavier atoms with core electrons (Li and B), the CMED is, in fact, close to the CMN, while this is not the case for D atoms (see supplemental material<sup>36</sup>). Refining the  $\text{LiBD}_4$  structure using combined SR-XPD and NPD data takes advantage of both radiations to accurately locate the heavier atoms B and Li thanks to their high x-ray scattering power (as explained, their CMED is close to their CMN) and to accurately locate the D atoms close to the CMN thanks to the high D neutron scattering power. The same holds true for atomic displacement parameters (ADP): If SR-XPD and NPD data are used, the contribution of atomic displacements to ADP mostly reflects nucleus displacements, i.e., of the CMN; if SR-XPD is used, the contribution of atomic displacements to ADP reflects displacements of the CMED. Additionally, ADP reflects not only averaged atomic displacements but also partly the deviation of the true scattering distribution from the IAM distribution (e.g., due to covalent bonds). The relative influence of these two contributions on the ADP may differ, depending on the data used for the refinement of the structural model and the type of atom. Therefore, unless the CMN and CMED are close to each other (e.g., atoms with a large valence/core electron ratio), significant differences between atomic coordinates and ADP obtained from the refinement of an IAM using SR-XPD or combined SR-XPD and NPD data may be expected for light atoms involved in covalent bonds.

Based on the previous discussion, it is very difficult to determine *a priori* the most appropriate prior distribution.

TABLE I. Prior and DFT density distributions and corresponding atomic integrated charges. X, structural model refined against x-ray data; XN, structural model refined against combined x-ray and neutron data; HR, high-resolution diffractometer; IP, image plate detector; Pos. I, DFT calculations with atomic position of case I; Pos. II, DFT calculations with atomic position of case II.

Case	Description	T (K)	Li (e)	B (e)	D1/D2/D3 (e)	BD <sub>4</sub> (e)
I	X-HR	10	2.17586	4.45427	1.38375/1.32234/1.33113	9.82262
II	XN-HR	10	2.21906	4.75303	1.30423/1.25548/1.23425	9.78124
III	X-HR	90	2.18810	4.44238	1.39047/1.33446/1.32265	9.81261
IV	XN-HR	90	2.23951	4.78615	1.30485/1.23030/1.21920	9.7597
V	X-IP	90	2.22578	4.51273	1.36064/1.28383/1.30606	9.76932
VI	XN-IP	90	2.25298	4.79397	1.31668/1.19753/1.21921	9.7466
DFT	Relaxed	0	2.1054	3.42514	1.63088/1.62774/1.60432	9.8924
DFT	Pos. I	0	2.09892	3.3155	1.65568/1.65298/1.63824	9.90064
DFT	Pos. II	0	2.10034	3.38928	1.63502/1.63026/1.61682	9.8882

As discussed, an IAM refined using combined SR-XPD and NPD data is the most appropriate choice for an accurate determination of the atomic structure (atomic positions and ADP corresponding closely to the ones for the real center of mass of the atoms). In an IAM refined using SR-XPD the interpretation of the ADP is not so straightforward (because of the deviation of the true scattering distribution from the IAM distribution discussed above); however, it provides atomic positions close to the CMED. It is, hence, likely that this prior distribution with individual atomic distributions centered on the CMED and ADP taking into account the combined effect of the thermal displacements and the deviation from the IAM distribution is better suited for an electronic distribution study. However, to fully verify this assertion, we need a reference system or data for the light complex hydrides that do not yet exist. Therefore, the differences observed between MEM distributions obtained based on the different prior distributions prevent any detailed discussion of fine bond features, especially for low-density regions like D atoms. Nevertheless, the MEM distributions are of sufficient quality to reliably extract integrated atomic charges from it, as will be discussed in Sec. III B for the LiBD<sub>4</sub> case study. The difference in the integrated atomic charges resulting from the use of different priors was, in

fact, used to determine the accuracy in a very conservative way.

The treatment of overlapping diffraction peaks using G constraints was sufficient to reduce the influence of the refined structural model used to extract the set of  $F_{\text{obs}}(\mathbf{H})$  to a level such that similar fine features of the electronic charge distributions are exhibited by MEM charge densities obtained for sets of  $F_{\text{obs}}(\mathbf{H})$  resulting from structural models refined using SR-XPD or combined SR-XPD and NPD data (see supplemental material<sup>36</sup>). The MEM distributions obtained based on these two possible refined IAMs (with and without use of G constraint) are illustrated in Fig. 1. No significant effect has been observed using high-order central moments for the distribution of the residuals of the structure factors (see Tables II and III and the supplemental material<sup>36</sup>). Because of the limited range of measured scattering angles ( $\sin\theta/\lambda \approx 0.6 \text{ \AA}^{-1}$ ), the priorly derived F constraints could not be considered (see Tables II and III and the supplemental material<sup>36</sup>).

In our attempt to compare results obtained for two different setups for the measurement of SR-XPD data (high-resolution diffractometer and image plate detector diffractometer), we found an excellent agreement between the final MEM

TABLE II. Summary of the MEM calculations at 10 K and corresponding atomic integrated charges.  $n$ , order of the statistical central moment  $\chi^n$  of normal residuals of the structure factors; G, Y if G constraint is used (125 reflections included in 36 G groups, 58 independent reflections); F-pc, Y if priorly derived F constraints are used.

Case	Description	$n$	G	F-pc	Prior	T (K)	Li (e)	B (e)	D1/D2/D3 (e)	BD <sub>4</sub> (e)
1.1	X-HR	2			I	10	2.160	4.009	1.512/1.460/1.429	9.839
1.2	X-HR	2	Y		I	10	2.135	3.910	1.497/1.563/1.446	9.862
1.3	X-HR	2	Y	Y	I	10	2.181	3.244	1.658/1.720/1.588	9.798
1.4	XN-HR	2			II	10	2.239	4.213	1.430/1.392/1.363	9.760
1.5	XN-HR	2			Uniform	10	2.379	3.298	1.391/1.482/1.451	9.073
1.6	XN-HR	2	Y		II	10	2.232	4.256	1.420/1.383/1.354	9.768
1.7	XN-HR	4	Y		II	10	2.225	4.277	1.430/1.375/1.346	9.774
1.8	XN-HR	6	Y		II	10	2.227	4.296	1.427/1.371/1.339	9.771
1.9	XN-HR	2	Y		Uniform	10	...	...	.../.../...	...
1.10	XN-HR	2	Y	Y	II	10	2.231	4.150	1.463/1.401/1.376	9.766
1.11	XN-HR	2	Y	Y	Uniform	10				

TABLE III. Summary of the MEM calculations at 90 K and corresponding atomic integrated charges. HR data with G constraint, 113 reflections included in 31 G groups, 71 independent reflections; IP data with G constraint, 140 reflections included in 36 G groups, 41 independent reflections.

Case	Description	$n$	G	F-pc	Prior	T (K)	Li (e)	B (e)	D1/D2/D3 (e)	BD <sub>4</sub> (e)
2.1	X-HR	2			III	90	2.176	4.092	1.490/1.450/1.396	9.825
2.2	X-HR	2	Y		III	90	2.154	4.091	1.516/1.465/1.386	9.845
2.3	X-HR	2	Y	Y	III	90	2.250	2.992	1.750/1.759/1.619	9.737
2.4	XN-HR	2			IV	90	2.240	4.329	1.397/1.344/1.344	9.757
2.5	XN-HR	2	Y		IV	90	2.237	4.395	1.364/1.325/1.338	9.760
2.6	XN-HR	4	Y		IV	90	2.224	4.421	1.374/1.304/1.338	9.774
2.7	XN-HR	6	Y		IV	90	2.223	4.442	1.375/1.292/1.333	9.774
2.8	XN-HR	2	Y	Y	IV	90	2.239	4.275	1.414/1.330/1.370	9.758
2.9	X-IP	2			V	90	2.198	4.158	1.461/1.360/1.410	9.799
2.10	X-IP	2	Y		V	90	2.170	4.308	1.466/1.359/1.347	9.826
2.11	X-IP	2	Y	Y	V	90	2.250	2.992	1.750/1.759/1.619	9.737
2.12	XN-IP	2			VI	90	2.235	4.295	1.438/1.297/1.368	9.767
2.13	XN-IP	2			Uniform	90	2.280	3.887	1.348/1.305/1.290	9.122
2.14	XN-IP	2	Y		VI	90	2.201	4.522	1.415/1.297/1.282	9.798
2.15	XN-IP	4	Y		VI	90	2.202	4.513	1.406/1.301/1.288	9.796
2.16	XN-IP	6	Y		VI	90	2.207	4.519	1.399/1.296/1.288	9.790
2.17	XN-IP	2	Y		Flat	90	2.208	4.029	1.281/1.077/0.965	8.317
2.18	XN-IP	2	Y	Y	VI	90	2.201	4.496	1.441/1.289/1.287	9.799
2.19	XN-IP	2	Y	Y	Uniform	90	2.208	4.029	1.281/1.077/0.965	8.317

distributions with G constraints corresponding to the two setups (see Figs. 2 and 3 and Table III). This simultaneously validates the collection of data using an image plate detector and the treatment of overlapped reflections by G constraints. As long as a good powder averaging is achieved in the sample, it is better to use data collected on a high-resolution diffractometer. The reason is the larger ratio of the number of independent reflections versus the number of reflections included in a G group for high-resolution data ( $\approx 60\%$  in the present case; see Table III) compared to image plate detector data ( $\approx 30\%$  in the present case; see Table III; note that the wavelength is different compared to high-resolution data). A larger number of independent reflections ensures a better independence of the  $F_{\text{obs}}(\mathbf{H})$  with respect to the chosen IAM model. Actually, for independent reflections, the IAM model only influences  $F_{\text{obs}}(\mathbf{H})$  through the scale factor needed to account for the data collection statistics. The lower resolution of an image plate detector increases the dependence of the MEM density distributions on the refined structure used for sharing the total intensity of a group of overlapped reflections among individual reflections (see the supplemental material<sup>36</sup>). However, the total intensity of a G group is, in fact, as independent of the IAM model as an individual independent reflection (see supplemental material<sup>36</sup>). Therefore, for samples with poor powder averaging, data collection of sufficient quality can be obtained by means of an image plate diffractometer (the whole Bragg rings are integrated, thus averaging the intensity as a good powder averaging would do).

### B. Density distribution of LiBD<sub>4</sub>

It is a general trend for all measurements (considering all temperatures and setups) that with respect to the prior distributions, part of the electronic charge of the B atom in

the IAM procrystal is redistributed over the D atoms in the MEM density distribution (see Figs. 2 and 3 and Table III). This trend emphasizes the additional information extracted from the data not contained in the IAM prior.

Comparing MEM distributions with G constraints, it appears that the charges determined by Bader analysis for the Li atom and the BD<sub>4</sub> group are less affected by the choice of the prior than the charges of the B and D atoms (compare Table I to Tables II and III). To understand this effect, one should keep in mind the weak density of D and the covalent nature of the B-D bond. In a simplified picture, any change in the prior distribution will affect the final density distribution, particularly the curvature of the density close to the border of the atomic basins (hence the shape of the zero-density flux surfaces determined by the Bader analysis). The effect on the size of two neighboring basins (and consequently on the integrated charge of the basins) may differ depending on the maximum charge of the basins and the charge at the border (zero-flux surface) between the two basins. For example, the ratio between the minimum of the density along the B-D bond and the maximum density of D is much larger than the ratio between the minimum of the density along the Li-B bond and the maximum density of Li (see Fig. 4). A change in the MEM distribution likely affects the critical points defining basins of atoms with a large ratio (e.g., between B and D) more than the critical points defining basins of atoms with a small ratio (e.g., between Li and B or Li and D), as illustrated in Fig. 4. One should, however, also keep in mind that a reasonably good prior density is still required since a uniform prior density may give quite different misleading results (see Tables II and III).

As a second general trend, MEM distributions based on a structural model refined using SR-XPD data systematically concentrate more charge on the D atoms than MEM

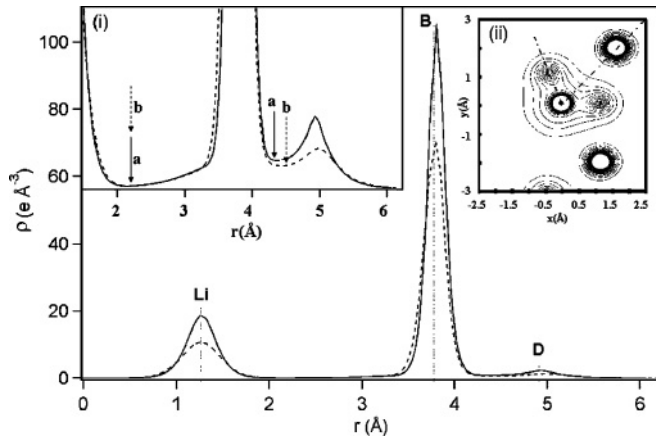


FIG. 4. Electronic density along the Li-B and B-D directions, indicated by the two dashed lines in inset (ii). Solid line shows MEM density distribution for data at 10 K with G constraints [prior distribution and  $F_{\text{obs}}(\mathbf{H})$  from SR-XPD refined model]; dashed line shows MEM density distribution for data at 10 K with G constraints [prior distribution and  $F_{\text{obs}}(\mathbf{H})$  from combined SR-XPD and NPD refined model]. In inset (ii), the minima of density along the lines are indicated by arrows qualitatively indicating the atomic basin separations (zero-density flux and bond critical point): (a) for MEM density distribution from the SR-XPD refined model and (b) for MEM density distribution from the combined SR-XPD and NPD refined model.

distributions based on a structural model refined using combined SR-XPD and NPD data (see Fig. 5). As discussed above and in the supplemental material,<sup>36</sup> this effect is a direct consequence of the influence of the prior density on the final MEM distribution (see the supplemental material<sup>36</sup>) and is due to the differences between the prior distributions that actually exhibit the same trend.

As expected, the difference between MEM distributions obtained at 10 K and at 90 K emphasizes the smearing effect of the increased thermal motion of the atoms at 90 K on the resulting MEM distributions (compare Figs. 2 and 3 to Fig. 1), although this effect has minor influence on the atomic charge obtained from applying the Bader analysis (see Tables II and III).

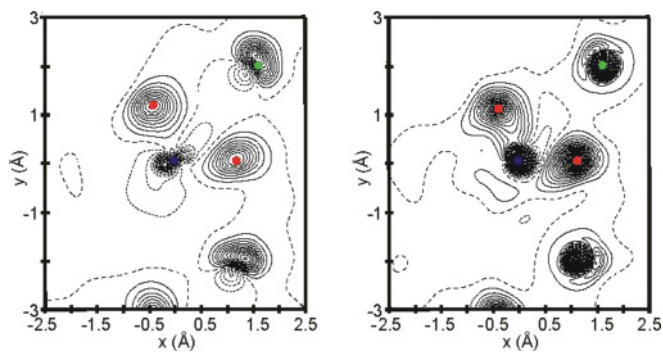


FIG. 5. (Color online) Difference (final minus prior) MEM density distribution for data at 10 K with G constraints. (left)  $F_{\text{obs}}(\mathbf{H})$  from combined SR-XPD and NPD refined model. (right)  $F_{\text{obs}}(\mathbf{H})$  from SR-XPD refined model. Contour intervals are  $0.02 \text{ e}/\text{\AA}^3$ . Plane cuts D1, D2, and B atoms; Li is green (light gray); B is blue (dark gray); D is red (medium gray).

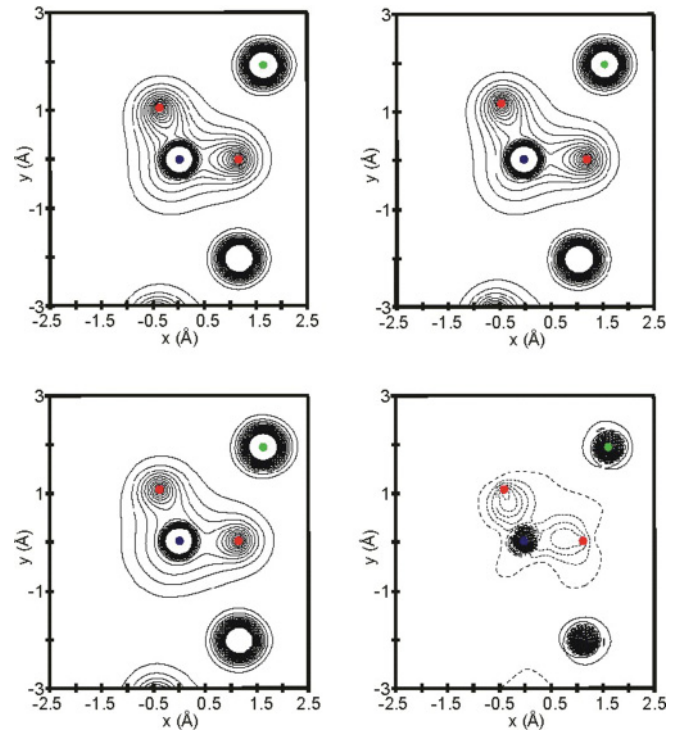


FIG. 6. (Color online) DFT density distributions: (top left) lattice and atomic coordinates from model refined with SR-XPD data at 10 K, (top right) lattice and atomic coordinates relaxed, (bottom left) MEM density distribution for data at 10 K with G constraints [ $F_{\text{obs}}(\mathbf{H})$  from SR-XPD refined model], and (bottom right) difference between MEM distribution and DFT distribution. Contour intervals are  $0.2 \text{ e}/\text{\AA}^3$ ; cutoff level is  $5 \text{ e}/\text{\AA}^3$ . Contour intervals for difference plot are  $0.1 \text{ e}/\text{\AA}^3$ . Plane cuts D1, D2, and B atoms; Li is green (light gray); B is blue (dark gray); D is red (medium gray).

Summarizing the different technical aspects discussed in this section, we conclude that for light tetrahydroborates (or, more generally, light hydrogen-based systems), the best MEM distribution based on SR-XPD data is obtained from the following: the use of high-resolution powder diffraction data, as long as a good powder averaging is not an issue; data collected at the lowest possible temperature (in the present case, 10 K); the use of a prior distribution obtained from an IAM refined using SR-XPD data; and the use of G constraint for strongly overlapping reflections.

Accordingly, the atomic charges of case 1.2 in Table II were considered to be the best experimental atomic charges. The experimental accuracy was determined from the difference between the extreme values of atomic charge (for each single atom) considering MEM distributions obtained at 10 and 90 K (for the two setups considered) with the different prior distributions (i.e., considering cases 1.2 and 1.6 in Table II and cases 2.2, 2.5, 2.10, and 2.18 onward in Table III). Since this estimate of the interval of accuracy does not correspond to the standard uncertainty (one sigma of a normal distribution), an additional “ $\pm$ ” was used inside the usual bracket notation of uncertainty to notify it. The experimental atomic/ionic charges are:  $\text{Li} = 2.14(\pm 9) \text{ e}$ ,  $\text{B} = 3.91(\pm 35) \text{ e}$ ,  $\text{D1} = 1.50(\pm 14) \text{ e}$ ,  $\text{D2} = 1.56(\pm 18) \text{ e}$ ,  $\text{D3} = 1.45(\pm 10) \text{ e}$ ,  $\text{BD}_4 = 9.86(\pm 9) \text{ e}$ .

As mentioned, no detailed discussion of the experimental electronic distribution was attempted. However, a couple of general observations may be discussed within the experimental accuracy. First, it has to be emphasized that the usual ionic picture of  $\text{LiBD}_4$  ( $\text{Li}^+$  cations and  $\text{BD}_4^-$  anions) with D covalently bonded to B holds. This is not only borne out in the experimental charge transfer of  $0.86 \pm 9$  e from Li atoms to  $\text{BD}_4$  groups but is also qualitatively visible in Fig. 4. Indeed, in Fig. 4 the charge density along the Li-B bond exhibits a minima close to  $\sim 0$  e/ $\text{\AA}^3$ , while the minimum of the density along the B-D bond is much larger (i.e., roughly half of the maximum density of D). This last observation holds, even when comparing the different density distributions obtained for the two considered priors. The difference between the two distributions at their minima along the B-D bond is indicated by arrows in Fig. 4 and is, in fact, much smaller than the total density at the same position. Finally, comparing experimental MEM density distributions to DFT calculations, as displayed in Fig. 6, it appears that the best agreement is obtained with the MEM density distribution obtained at 10 K with a prior density distribution from an IAM model refined using SR-XPD data (see Fig. 1 and Table II). This further reinforces our deduction of the best experimental distribution among the ones calculated in this work.

#### IV. CONCLUSION

The atomic and ionic charge density of  $\text{LiBD}_4$  has been experimentally determined using synchrotron radiation x-ray powder diffraction data and the maximum entropy method (MEM). The best MEM distribution was obtained from high-resolution synchrotron radiation x-ray powder diffraction (SR-XPD) data collected at 10 K and MEM calculations using G constraint for strongly overlapping reflections and a prior distribution obtained from an IAM refined using

SR-XPD data. The experimental atomic and ionic charges are:  $\text{Li} = 2.14(\pm 9)$  e,  $\text{B} = 3.91(\pm 35)$  e,  $\text{D1} = 1.50(\pm 14)$  e,  $\text{D2} = 1.56(\pm 18)$  e,  $\text{D3} = 1.45(\pm 10)$  e,  $\text{BD}_4 = 9.86(\pm 9)$  e. The corresponding charge transfer from the Li cation to the  $\text{BD}_4$  anion is of  $0.86(\pm 9)$  e, in very good agreement with the value of  $0.895$  e calculated by the density functional theory and the usual ionic picture of  $\text{LiBH}_4$ . The role of the prior density distribution for the calculation of the MEM density distributions has been carefully investigated and provided a way to determine the experimental accuracy of the atomic and ionic charges. An excellent consistency has been observed between experimental results obtained for data collected at 10 and 90 K, considering different experimental setups (high-resolution diffractometer or image plate diffractometer) and different structural models used for the prior density distributions (refined using only SR-XPD data or using SR-XPD data combined with neutron powder diffraction data). This reinforces the validity of the approach considered in this work to determine experimental density distributions, which may be extended to many other light hydrogen-based systems. It also demonstrates the possibility of collecting SR-XPD data with an image plate detector diffractometer, opening a window to possible fast measurements (order of magnitude of a few minutes), allowing us to scan many temperature conditions.

#### ACKNOWLEDGMENTS

We highly appreciated skillful assistance from F. Gozzo at the MS beamline at the SLS (PSI, Villigen, Switzerland) and D. Sheptyakov at the HRPT instrument at the SinQ (PSI, Villigen, Switzerland). CPU time allocation at CSCS supercomputer center (Manno) is kindly acknowledged. Financial support from Swiss National Science Foundation (Schweizerischer Nationalfonds, SNF) Project No. 200020-115875 is gratefully acknowledged.

\*Also at Physics Department, University of Fribourg, CH-1700 Fribourg, Switzerland; florian.buchter@empa.ch

†Also at Physics Department, University of Fribourg, CH-1700 Fribourg, Switzerland.

<sup>1</sup>L. Schlapbach and A. Züttel, *Nature (London)* **414**, 353 (2001).

<sup>2</sup>W. Grochala and P. Edwards, *Chem. Rev.* **104**, 1283 (2004).

<sup>3</sup>A. Züttel, A. Borgschulte, and S. Orimo, *Scr. Mater.* **56**, 823 (2007).

<sup>4</sup>S. Orimo, Y. Nakamori, J. Eliseo, A. Züttel, and C. M. Jensen, *Chem. Rev.* **107**, 4111 (2007).

<sup>5</sup>A. Züttel, A. Borgschulte, and L. Schlapbach, *Hydrogen as a Future Energy Carrier* (Wiley, Hoboken, NJ, 2008).

<sup>6</sup>Y. Filinchuk, D. Chernyshov, and V. Dmitriev, *Z. Kristallogr.* **223**, 649 (2008).

<sup>7</sup>Y. Nakamori, H. W. Li, K. Miwa, S. Towata, and S. Orimo, *Mater. Trans.* **47**, 1898 (2006).

<sup>8</sup>Y. Nakamori, K. Miwa, A. Ninomiya, H. Li, N. Ohba, S. I. Towata, A. Züttel, and S. Orimo, *Phys. Rev. B* **74**, 045126 (2006).

<sup>9</sup>A. J. Du, S. C. Smith, and G. Q. Lu, *Phys. Rev. B* **74**, 193405 (2006).

<sup>10</sup>Z. Łodziana, A. Züttel, and P. Zielinski, *J. Phys. Condens. Matter* **20**, 465210 (2008).

<sup>11</sup>E. A. Nickels, M. O. Jones, W. I. F. David, S. R. Johnson, R. L. Lowton, M. Sommariva, and P. Edwards, *Angew. Chem. Int. Ed.* **47**, 2817 (2008).

<sup>12</sup>E. T. Jaynes, *Phys. Rev.* **106**, 620 (1957).

<sup>13</sup>S. F. Gull and G. J. Daniel, *Nature (London)* **272**, 686 (1978).

<sup>14</sup>D. M. Collins, *Nature (London)* **298**, 49 (1982).

<sup>15</sup>M. Sakata and M. Sato, *Acta Crystallogr. Sec. A* **46**, 263 (1990).

<sup>16</sup>C. J. Gilmore, *Acta Crystallogr. Sec. A* **52**, 561 (1996).

<sup>17</sup>B. Bagautdinov, J. Luedecke, M. Schneider, and S. van Smaalen, *Acta Crystallogr. Sec. B* **54**, 626 (1998).

<sup>18</sup>R. E. Dinnebier, M. Schneider, S. Van Smaalen, F. Olbrich, and U. Behrens, *Acta Crystallogr. Sec. B* **55**, 35 (1999).

<sup>19</sup>T. Noritake, M. Aoki, S. Towata, Y. Seno, Y. Hirose, E. Nishibori, M. Takata, and M. Sakata, *Appl. Phys. Lett.* **81**, 2008 (2002).

<sup>20</sup>M. Merli and A. Pavese, *Z. Kristallogr.* **221**, 613 (2006).

<sup>21</sup>P. Roversi, J. J. Irwin, and G. Bricogne, *Acta Crystallogr. Sec. A* **54**, 971 (1998).

<sup>22</sup>W. Jauch and A. Palmer, *Acta Crystallogr. Sec. A* **49**, 590 (1993).

<sup>23</sup>W. Jauch, *Acta Crystallogr. Sec. A* **50**, 650 (1994).

<sup>24</sup>B. B. Iversen, F. K. Larsen, M. Souhassou, and M. Takata, *Acta Crystallogr. Sec. B* **51**, 580 (1995).

- <sup>25</sup>R. Y. de Vries, W. J. Briels, and D. Feil, *Phys. Rev. Lett.* **77**, 1719 (1996).
- <sup>26</sup>L. Palatinus and S. van Smaalen, *Acta Crystallogr. Sec. A* **58**, 559 (2002).
- <sup>27</sup>L. Palatinus and S. van Smaalen, *Acta Crystallogr. Sec. A* **61**, 363 (2005).
- <sup>28</sup>V. Dmitriev, Y. Filinchuk, D. Chernyshov, A. V. Talyzin, A. Dzwilewski, O. Andersson, B. Sundqvist, and A. Kurnosov, *Phys. Rev. B* **77**, 174112 (2008).
- <sup>29</sup>R. F. W. Bader, *Atoms in Molecules: A Quantum Theory* (Clarendon, Oxford, 1990).
- <sup>30</sup>F. Buchter, Z. Łodziana, Ph. Mauron, A. Remhof, O. Friedrichs, A. Borgschulte, A. Züttel, D. Sheptyakov, T. Strässle, and A. J. Ramirez-Cuesta, *Phys. Rev. B* **78**, 094302 (2008).
- <sup>31</sup>J.-Ph. Soulié, G. Renaudin, R. Černý, and K. Yvon, *J. Alloys Compd.* **346**, 200 (2002).
- <sup>32</sup>A. Züttel, S. Rentsch, P. Fisher, P. Wenger, P. Sudan, Ph. Mauron, and Ch. Emmenegger, *J. Alloys Compd.* **356-357**, 515 (2003).
- <sup>33</sup>M. Hartman, J. Rush, T. Udovic, R. Bowman Jr., and S.-J. Hwang, *J. Solid State Chem.* **180**, 1298 (2007).
- <sup>34</sup>Y. Filinchuk, D. Chernyshov, and R. Černý, *J. Phys. Chem. C* **112**, 10579 (2008).
- <sup>35</sup>J. Rodríguez-Carvajal, *Physica B* **192**, 55 (1993).
- <sup>36</sup>See supplemental material at [<http://link.aps.org/supplemental/10.1103/PhysRevB.83.064107>] for detailed information on (A) the Rietveld refinements, (B) the influence of the refined structural model on the sharing of the total intensity for overlapping reflections, with and without G-constraints, (C) the influence of prior density distribution considering different structural models for a given set of  $F_{\text{obs}}(\text{H})$ , (D) the influence of the order of the statistical central moment of the normal residuals of the structure factors and (E) the Influence of the use of prior-derived F constraints.
- <sup>37</sup>Electron densities of neutral atoms from an IAM model convoluted with occupation probability distribution corresponding to the refined atomic thermal displacements.
- <sup>38</sup>S. van Smaalen, L. Palatinus, and M. Schneider, *Acta Crystallogr. Sec. A* **59**, 459 (2003).
- <sup>39</sup>Overlapping reflections not resolved for intensities above half of the reflection maxima.
- <sup>40</sup>M. Sakata, R. Mori, S. Kumazawa, M. Takata, and H. Toraya, *J. Appl. Crystallogr.* **23**, 526 (1990).